ADVANCED MATERIALS
www.advmat.de

CO_2 Adsorption in a Robust Iron(III) Pyrazolate-Based MOF: Molecular-Level Details and Frameworks Dynamics From Powder X-ray Diffraction Adsorption Isotherms

Rebecca Vismara, Stephanie Terruzzi, Angelo Maspero, Toni Grell, Filippo Bossola, Angelo Sironi, Simona Galli, Jorge A. R. Navarro, and Valentina Colombo**

Understanding adsorption processes at the molecular level, with multi-technique approaches, is nowadays at the frontier of porous materials research. In this work it is shown that with a proper data treatment, in situ high-resolution powder X-ray diffraction (HR-PXRD) at variable temperature and gas pressure can reveal atomic details of the accommodation sites, the framework dynamics as well as thermodynamic information (isosteric heat of adsorption) of the CO_2 adsorption process in the robust iron(III) pyrazolate-based MOF $Fe_2(BDP)_3$ [H_2BDP = 1,4-bis(1*H*-pyrazol-4-yl)benzene]. Highly reliable "HR-PXRD adsorption isotherms" can be constructed from occupancy values of CO_2 molecules. The "HR-PXRD adsorption isotherms" accurately match the results of conventional static and dynamic gas sorption experiments and Monte Carlo simulations. These results are indicative of the impact of the molecular-level behavior on the bulk properties of the system under study and of the potential of the presented multi-technique approach to understand adsorption processes in metal–organic frameworks.

1. Introduction

The properties and applications of porous materials are strictly related to the size, shape, decoration and accessibility of their pores.[1] For this reason, many efforts have been spent in finding appropriate techniques to properly characterize the pore surface.[2,3] Gas adsorption isotherms, where the uptake of a probe molecule (typically N_2) is recorded as a function of its partial pressure at a certain temperature,[3,4] are worldwide recognized as the par excellence technique to characterize porous solids.[2,5] By using the experimental macroscopic pressure–loading curves, the underlying atomic-level adsorbent-adsorbate interactions can be inferred according to necessarily approximated models.[3]

However, an in-depth understanding of the adsorption process, by unveiling the hidden host–guest/guest–guest interactions and the framework dynamics, is necessary to develop new cutting-edge materials. This kind of studies are more challenging and usually require in situ monitoring of the adsorption process. Different techniques have been proposed to this aim, ranging from nuclear magnetic resonance (NMR)[3,6–8] to inverse gas chromatography (IGC-FC),[9,10] structural and spectroscopic methods and theoretical simulations.[11–19]

In the recent years, in situ and operando synchrotron radiation high-resolution powder X-ray diffraction (HR-PXRD) experiments have been considered a powerful tool to unveil the main interactions and primary adsorption sites[16,20–22] in a wide range of inorganic,[17,23,24] organic,[25,26] and metal–organic porous materials.[15,16,27,28] Despite these multiple examples, the information obtained so far were limited to the localization of the guest molecules and the modification of the host framework. Only recently,[16,17,29] some efforts to model and understand the whole adsorption process have been made, including the construction of adsorption isotherms. However, this approach has not yet been stretched to the limit, going beyond crystal structure determination, host–guest interactions description, and guest quantification, to study additional properties, such as the thermodynamics of the adsorption process. In this work, we show that a plethora of hidden but easily accessible information can be extracted from, nowadays underexploited, PXRD data

R. Vismara, A. Maspero, S. Galli
Dipartimento di Scienza e Alta Tecnologia
Università degli Studi dell'Insubria
Via Valleggio 11, Como 22100, Italy
R. Vismara, J. A. R. Navarro
Departamento de Química Inorgánica
Universidad de Granada
Av. Fuentenueva S/N, Granada 18071, Spain
E-mail: jarn@ugr.es
S. Terruzzi, T. Grell, A. Sironi, V. Colombo
Dipartimento di Chimica
Università degli Studi di Milano
Via Golgi 19, Milano 20133, Italy
E-mail: valentina.colombo@unimi.it
F. Bossola, V. Colombo
CNR – Istituto di Scienze e Tecnologie Chimiche "Giulio Natta"
Via Golgi 19, Milan 20133, Italy
S. Galli, V. Colombo
Consorzio Interuniversitario Nazionale per la Scienza e Tecnologia dei Materiali
Via Giusti 9, Firenze 50121, Italy
The ORCID identification number(s) for the author(s) of this article can be found under https://doi.org/10.1002/adma.202209907.

DOI: 10.1002/adma.202209907

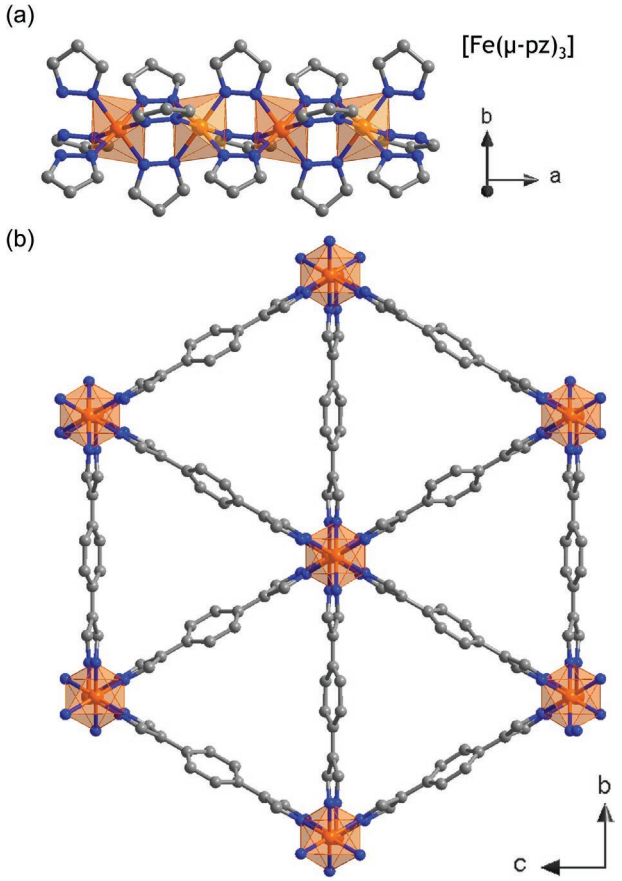

Figure 1. a,b) Representation of a portion of a μ-pyrazolate-bridged chain of octahedral iron(III) ions (a) and the crystal structure of $Fe_2(BDP)_3$ viewed along the [100] crystallographic direction (b) (*Fddd*, $a = 7.1046(2)$ Å, $b = 26.4943(5)$ Å, $c = 45.3489(9)$ Å, $V = 8536.1(4)$ Å^3). Hydrogen atoms are omitted for clarity. Color codes: Fe, orange; N, blue; C, grey. Crystallographic information from.[33]

without the necessity to recur to more sophisticated X-ray based techniques, or to rely on single-crystals.[19,30–32] With this aim, we have performed an in-depth HR-PXRD characterization of the CO_2 adsorption process in the robust pyrazolate-based $Fe_2(BDP)_3$ [H_2BDP = 1,4-bis(1*H*-pyrazol-4-yl)benzene] system (**Figure 1**).[33] We have compared the behaviour of $Fe_2(BDP)_3$ at the molecular level (diffraction experiments and computational modelling) with the results obtained for the bulk properties (adsorption experiments), aiming to show that PXRD, applied on variable gas pressure data sets, should not be exclusively seen as a way to localize the adsorbed guest molecules in the host framework, but also as a mean to shed light on the thermodynamics of the process.

2. Results and Discussion

2.1. Preliminary Considerations on $Fe_2(BDP)_3$ Crystal Structure, Chemical and Thermal Stability

$Fe_2(BDP)_3$ is a highly chemically and thermally robust MOF, consisting of 1D μ-pyrazolate-bridged chains of octahedral iron(III) nodes (Figure 1a), connected in three dimensions by the BDP^{2-} linkers. This linkage yields a rigid framework with triangular 1D channels (Figure 1b).[33] $Fe_2(BDP)_3$ has been recently recognized as one of the most chemically stable MOFs reported so far.[34] Its high chemical stability, already demonstrated for other pyrazolate-based MOFs,[16,35–37] can be related to the strong, charge assisted, Fe^{III}–N bonds and the highly connected crystal structure.[38,39] Considering the relevance of the thermal and chemical stability of MOFs when industrial applications are sought,[40] particularly for CO_2 separation processes, we have complemented the available data on the chemical stability with the characterization of the thermal properties, performing a variable-temperature powder X-ray diffraction (VT-PXRD) experiment, up to thermal decomposition, coupled to a simultaneous thermal analysis (STA).[41] As shown by STA and VT-PXRD (see Figures S1 and S2 in the Supporting Information),[33] $Fe_2(BDP)_3$ is stable up to 723 K without collapsing or undergoing any phase transition during the desolvation process, experiencing only a limited unit cell volume increase by 0.3%, mainly due to the slight enlargement of the *a*-axis, which is strictly related to the distance between the Fe^{III} centres along the 1D chains, running parallel to the [100] direction. Indeed, the μ-pyrazolate ring bridges two metal ions at rather short distances (3.5–3.7 Å),[16,33] limiting more pronounced structural deformations, thus confirming the rigid nature of the framework.

2.2. In Situ High-Resolution Powder X-ray Diffraction Adsorption Studies

2.2.1. Unit Cell Parameters Variation as a Function of CO_2 Loading

We have proceeded with a detailed study of the CO_2 adsorption process in $Fe_2(BDP)_3$ by means of in situ high-resolution powder X-ray diffraction (HR-PXRD) at variable pressure and temperature. Whole powder pattern refinements[42] were performed on the data acquired at 273 and 298 K in the CO_2 pressure range of 0–8 bar (see **Figure 2**a; Figure S9, Supporting Information). The framework shows, in spite of its rigidity, a plastic response to the CO_2 pressure stimuli (Figure 2b; Tables S5–S8, Supporting Information). Namely, a unit cell volume contraction between 0 and 1 bar of CO_2 ($\Delta V/V_0 \approx 0.04\%$ at $T = 273$ K and $\Delta V/V_0 < 0.05\%$ at $T = 298$ K) is followed by a slight increase up to 8 bar ($\Delta V/V_0 = 0.26\%$ at $T = 273$ K and $\Delta V/V_0 = 0.16\%$ at $T = 298$ K, see Figure 2b and Figure S11, Supporting Information). The crystallographic *a*-axis plays a main role in the described phenomena: at 273 K, this axis undergoes a decrease by ≈0.02% between 0 and 1 bar, followed by a slight increase of ≈0.17% at 8 bar of CO_2. On the contrary, the *b*- and *c*-axis increase by only ≈0.05% at 8 bar. The initial unit cell volume shrinkage at pressures lower than 1 bar was already described for other MOF systems through HR-PXRD[16,33] or the in-depth analysis of the X-ray scattering profiles during gas adsorption experiments.[30] This phenomenon was termed "organization point" of the adsorption isotherm, and related to the formation of a superlattice of adsorbates with different amounts in adjacent pores.[30]

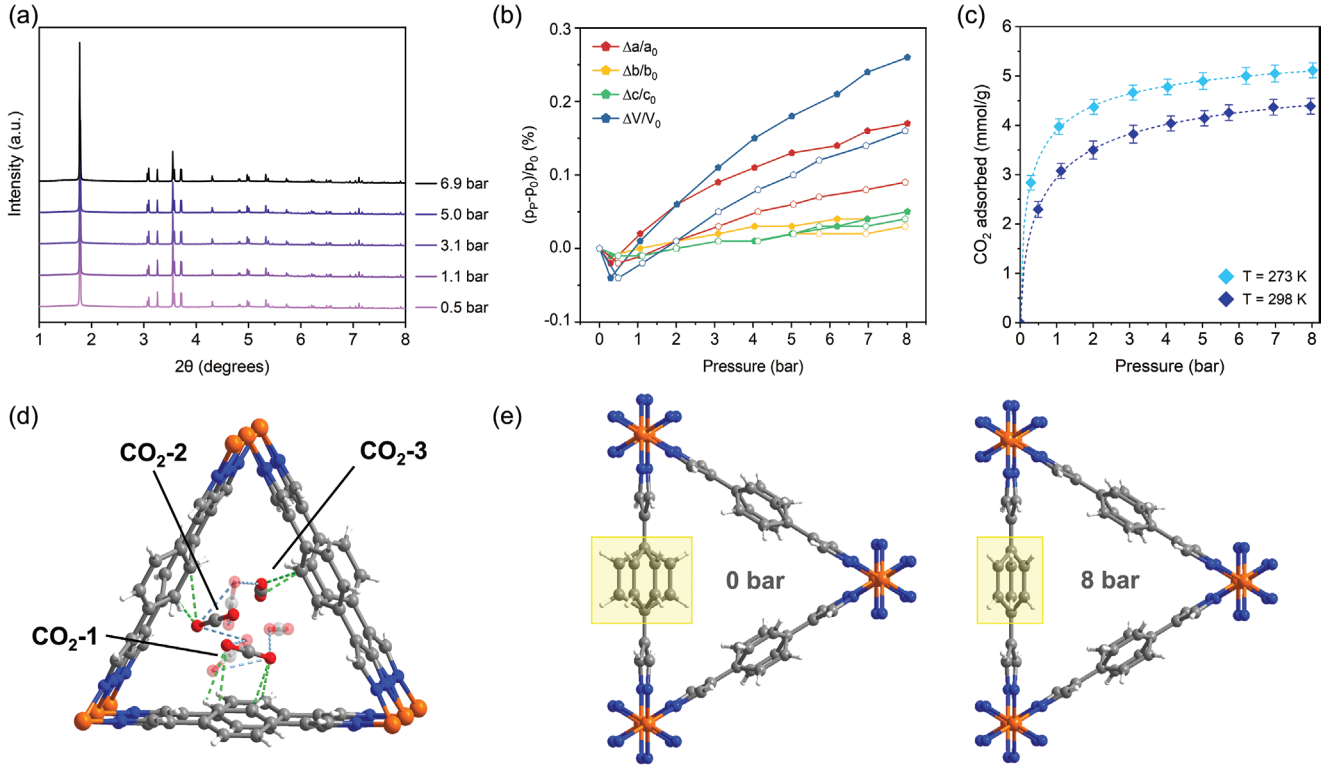

Figure 2. a) Selection of HR-PXRD patterns acquired at 298 K and variable CO_2 pressure in the 1°–8° 2θ range. The complete set of collected data can be found in Figure S9 in the Supporting Information. b) Relative percentage variation of the unit cell parameters (p_p) at 273 K (full symbols) and 298 K (open symbols) with respect to the values at $p_{CO2} = 0$ bar (p_0). The lines have been added to guide the eye. c) Adsorption isotherms extracted after Rietveld refinements in the range 0–8 bar at 273 and 298 K. The dashed lines depict the fit obtained using the Freundlich–Langmuir model. d) Position of the three independent CO_2 molecules, together with the main host–guest (green dashed lines) and guest–guest (light blue dashed lines) interactions, obtained from the Rietveld refinement at 273 K and $p_{CO2} = 1$ bar; the central ring of the ligands has been ordered for clarity. e) Torsion variation of the phenyl ring of one of the two independent ligands in response to CO_2 loading.

2.2.2. Location of the CO_2 Adsorption Sites and Identification of the Structural Parameters Depending on CO_2 Loading

To localise the CO_2 primary adsorption sites and quantify the amount of gas adsorbed, ab initio structure determinations followed by Rietveld refinements were successfully performed on the HR-PXRD data (Figure S8, Supporting Information). Three primary adsorption sites with different occupancy were identified in the range 0–8 bar and at 273/298 K. Hence, three crystallographically independent CO_2 molecules were located inside the triangular channels, namely: CO_2-1, CO_2-2, and CO_2-3, see Figure 2d and Figures S12 and S13 (Supporting Information). The three adsorption sites are active at all the studied pressures and temperatures; only a slight variation in the orientation of the guest molecules was observed during CO_2 loading. Two different types of host–guest interactions were found: side-on interactions were observed for CO_2-1 and CO_2-3 where both the oxygen atoms interact with the C–H bonds of the central ring of the ligand ($C–H_{ligand}\cdots O_{CO2}$ = 1.8–2.6 Å; Tables S9 and S10, Supporting Information), whereas CO_2-2 interacts with the C–H bonds of the ligand central ring in an end-on mode ($C–H_{ligand}\cdots O_{CO2}$ = 1.7 Å), see Figure 2d and Tables S9 and S10 in the Supporting Information. These interactions are found both in a single triangular mesh and in adjacent ones, in agreement with the nature of the pores of this system (1D channels) where CO_2 molecules can diffuse through. In addition, guest–guest interactions between the different CO_2 molecules were observed in the range 2.5–2.9 Å (Figure 2d; Tables S9 and S10, Supporting Information). Interestingly, both at 273 and 298 K, the applied CO_2 pressure affected the rotation and the disorder of the central ring of one of the two crystallographically independent ligands (see Figure 2e; Tables S11 and S12, Supporting Information): this occurrence can be explained by the described $O_{guest}\cdots CH_{host}$ interactions and it is indicative of the adaptative nature of the $Fe_2(BDP)_3$ framework which, despite its overall rigidity, can behave as a flexible material, being able to respond to the external stimuli induced by the CO_2 pressure, by adapting its pores through phenyl ring rotations. The amount of CO_2 adsorbed increases applying higher pressures and is inversely proportional to the adsorption temperature, as expected. The occupancies of CO_2-1, CO_2-2, and CO_2-3 as a function of the applied pressure are reported in Figure S14 and Tables S13 and S14 in the Supporting Information. The occupancies follow the trend CO_2-3 > CO_2-1 > CO_2-2, indicating that side-on interactions with benzene residues (CO_2-3, CO_2-1) are preferred over the end-on configuration (CO_2-2).

2.2.3. Construction of CO_2 HR-XRPD Adsorption Isotherms

The summation of the CO_2 occupancies obtained by Rietveld refinements on the entire set of data were used to construct the CO_2 "HR-PXRD adsorption isotherms" for both the essayed temperatures (Figure 2c). In the experimental conditions used for the HR-PXRD adsorption isotherms, $Fe_2(BDP)_3$ adsorbs 3.98 and 3.08 mmol g^{-1} of CO_2 at 273 and 298 K and 1 bar and up to 5.12 and 4.39 mmol g^{-1} at 273 and 298 K and 8 bar, respectively. Interestingly, the Freundlich–Langmuir model[43] was successfully applied to the HR-PXRD adsorption isotherms in the range 0–8 bar and at both temperatures (273 and 298 K) (Figure 2c). The modelled isotherms were then used, for the first time, to calculate the isosteric heat of adsorption (Q_{st}) by applying the Clausius–Clapeyron equation (see **Figure 3**).[43] Notably, the absolute values of Q_{st} monotonically increase with increasing guest loading from −30.7 kJ mol^{-1} at 3.0 mmol g^{-1} to −33.1 kJ mol^{-1} at 4.0 mmol g^{-1}. This is an unusual behavior for a porous material, spanning a wide range of pressure values (up to 8 bars) and might be indicative of cooperative adsorption, possibly related to favorable guest–guest interactions and the adaptive nature of the 1D channels in $Fe_2(BDP)_3$ (see above). Moreover, the Q_{st} values retrieved from HR-PXRD adsorption isotherms are in a very good agreement with those obtained from the conventional adsorption isotherms (see below, Figure 3). These results are indicative of the impact of the molecular-level behavior on the bulk properties of the system under study and of the robustness of the CO_2 HR-PXRD adsorption isotherms method.

2.3. Conventional Static and Dynamic Adsorption Studies

In order to further evaluate the suitability of the $Fe_2(BDP)_3$ system for CO_2 capture and to confirm the robustness of the CO_2 HR-PXRD adsorption isotherms approach, we have carried out conventional single component adsorption isotherms and advanced dynamic experiments (breakthrough curve measurements) in the 195–323 K temperature range (**Figure 4**; Figure S5, Supporting Information). Noteworthy, the static CO_2 adsorption isotherms in the 0–1 bar pressure range clearly correlate to the HR-PXRD adsorption isotherms with deviations that relate to the different experimental conditions, with shorter equilibration times in the case of the HR-PXRD experiment (see the Experimental Section). The calculated Q_{st} values, using the Claussius–Clapeiron equation, are provided in Table S1 (Supporting Information) and depicted in Figure 3. Similarly to the data derived from the CO_2 HR-PXRD adsorption isotherms, the absolute values of Q_{st} monotonically increase with increasing guest loading from −28.3(3) kJ mol^{-1} at 0.20 mmol g^{-1} to −31.8(14) kJ mol^{-1} at 3.82 mmol g^{-1}. It should be highlighted here again that, at the same CO_2 loading, the Q_{st} value calculated from HR-PXRD adsorption isotherms matches very well the one determined from conventional adsorption isotherms, being −32.16 kJ mol^{-1} at 3.80 mmol g^{-1} (Table S1, Supporting Information). This behavior contrasts the previous results obtained on the isoreticular $Fe_2(BPEB)_3$ [H_2BPEB = 1,4-bis(1*H*-pyrazol-4-ylethynyl)benzene][16] system, in which wider 1D triangular pores (18 Å edges) give rise to a lower and constant Q_{st} value of −26 kJ mol^{-1} (calculated from volumetric adsorption isotherms only).[16] The unusual CO_2 behavior in the $Fe_2(BDP)_3$ pores prompted us to evaluate its ability for CO_2 separation from flue gas. With this aim, we have registered the N_2 adsorption isotherms at 273 and 298 K (Figure 4a), which allowed to calculate the CO_2/N_2 ideal adsorbed solution theory (IAST) selectivity.[44] The calculated partition coefficients α_{CO_2/N_2} for a mixture of N_2:CO_2 (in 85:15 v/v ratio, to simulate the flue gases emitted by a power plant) are 23 and 22 at 273 and 298 K, respectively.

To assess the actual CO_2 adsorption capacity and selectivity over interferents, a mixture of N_2:CO_2 (in 85:15 v/v ratio) was passed through a column packed with $Fe_2(BDP)_3$ at different temperatures (T = 273/303/323/353 K). At the essayed experimental conditions, the strongest interactions of the material take place with the quadrupolar CO_2 molecule, which is efficiently sequestrated, while N_2 is not retained, see Figure 4b. As expected, the CO_2 retention time and, consequently, the adsorption capacity are inversely proportional to the acquisition temperature, passing from 1.46 mmol g^{-1} of MOF at 273 K to 0.35 mmol g^{-1} at 353 K (Table S3, Supporting Information).

$Fe_2(BDP)_3$ recyclability was then evaluated by means of iterative adsorption-desorption cycles. The MOF can undergo at least 11 temperature swing adsorption cycles (T = 303–393 K), with no performance loss (Figure 4c; Figure S7a and Table S4, Supporting Information) and no evidence of decrease of crystallinity (PXRD evidence, Figure S7b, Supporting Information).

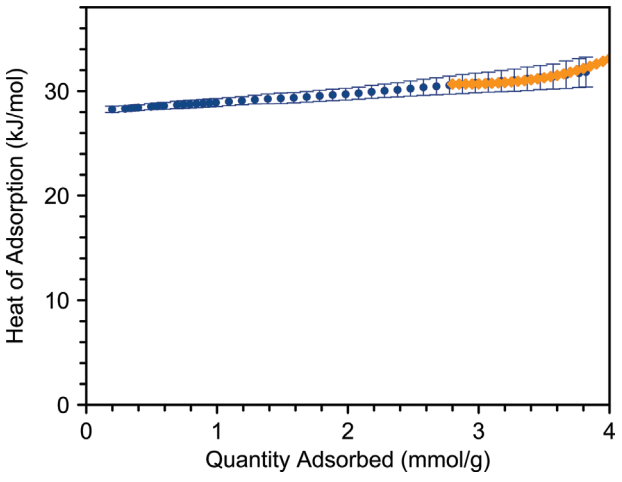

Figure 3. Comparison between the isosteric heats of adsorption (Q_{st}) as a function of the CO_2 uptake for $Fe_2(BDP)_3$ calculated from the conventional adsorption isotherms (blue circles) and retrieved from the HR-PXRD experiment (orange diamonds).

2.4. Monte Carlo Simulations

The use of computational methods can help in understanding the adsorption process at the atomic level, thus complementing experimental observations.[45] The CO_2 adsorption isotherms at 273 and 298 K were simulated in the range 0–8 bar, using the software Materials Studio,[46] and they were compared to both the experimental ones (p_{CO2} = 0–1 bar) and those retrieved from HR-PXRD data treatment (p_{CO2} = 0–8 bar), see **Figure 5**a. The

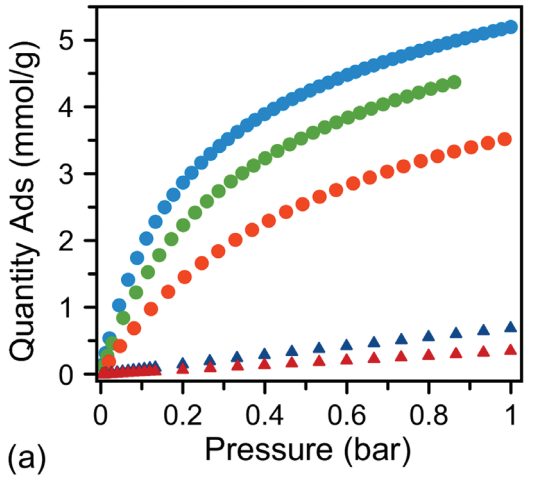

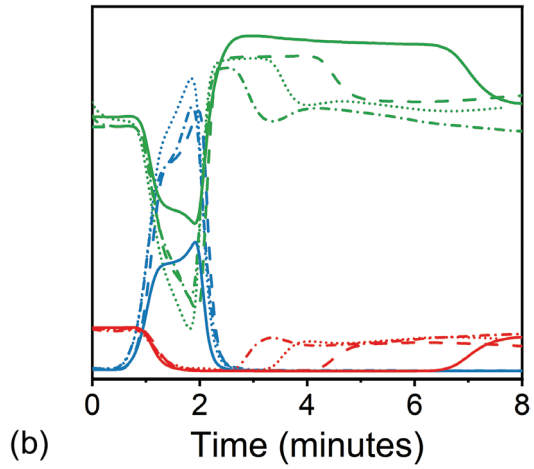

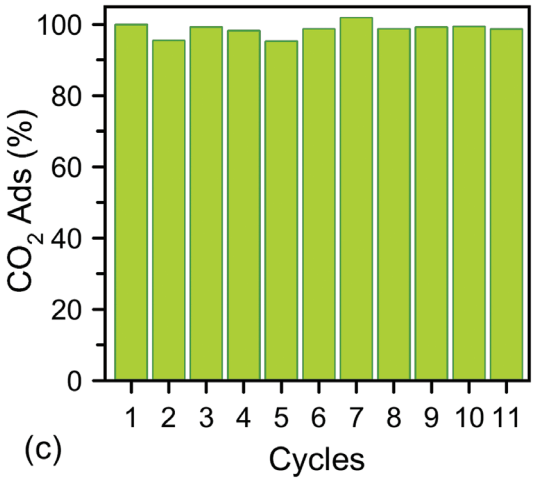

Figure 4. a) CO_2 adsorption isotherms at $T = 273$ (light blue circles), 283 (green circles), and 298 K (red circles) and N_2 adsorption isotherms at $T = 273$ (blue triangles) and 298 K (dark red triangles). b) Graphical output of the breakthrough curves measured at different temperatures ($T = 273$ K solid line, $T = 303$ K dashed line, $T = 323$ K dotted line and $T = 353$ K dash-dotted line). Color code: He blue trace, N_2 green trace and CO_2 red trace. c) Percentage variation of the CO_2 adsorption capacity of $Fe_2(BDP)_3$ over 11 consecutive cycles with respect to cycle 1.

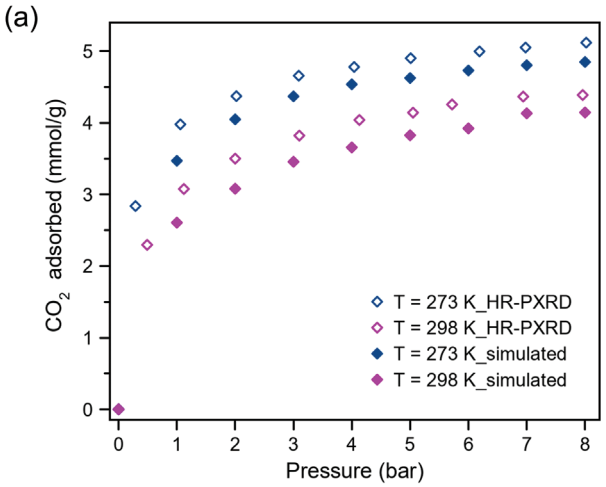

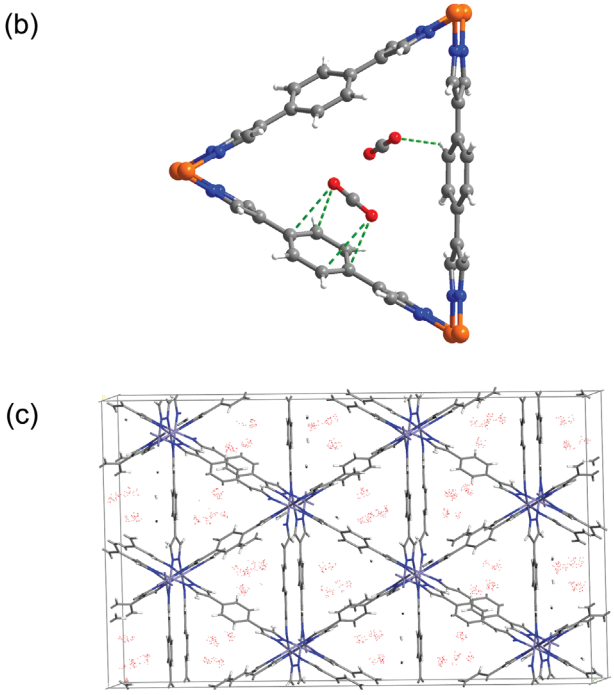

Figure 5. a) Comparison of the CO_2 adsorption isotherms retrieved from computational modelling and calculated from HR-PXRD at 273 and 298 K. b) Representation of the main host–guest interactions retrieved from the MC simulation. c) Representation of the center of mass probability density of the CO_2 molecules per unit cell of $Fe_2(BDP)_3$ viewed approximately along the [100] direction, as determined from the MC simulation at 273 K.

results of the simulation are in good agreement with the experimental HR-PXRD adsorption isotherms, further confirming the robustness of the multi-technique approach. The small deviations should be related to the rigid nature of the structural model used in the computational simulations versus the slightly plastic nature of the $Fe_2(BDP)_3$ framework.

Figure 5b,c shows the main host–guest interactions and the centre of mass of the calculated CO_2 adsorption sites at 273 K, respectively. All the configurations can be found in Figures S15 and S16 in the Supporting Information. The simulations confirmed what retrieved from HR-PXRD: the carbon

dioxide molecules interact with the walls of the triangular channels in two different ways, namely by using: (i) both the oxygen atoms in side-on mode, with $C–H_{ligand}\cdots O_{CO2}$ interactions in the range 2.7–3.5 Å with the carbon atoms of the phenyl ring of the ligand, or (ii) only one oxygen atom, in an end-on mode ($C–H_{ligand}\cdots O_{CO2} = 2.9$ Å). These two different configurations are in good agreement with what has been experimentally observed for the couple CO_2-1/CO_2-3 and for CO_2-2, respectively.

3. Conclusion

The described multi-technique approach, in which in situ HR-PXRD, static and dynamic adsorption experiments, and computational modelling are combined, is suited for understanding the complex and efficient accommodation of CO_2 molecules in the unusual triangular 1D pores of the $Fe_2(BDP)_3$ framework. An in-depth data treatment of the HR-PXRD adsorption data has been performed to unveil the details of the adaptive nature of the pores of $Fe_2(BDP)_3$, which is considered to be a "rigid" system. Moreover, the "HR-PXRD adsorption isotherms" retrieved at different temperatures allowed to extract, besides crystallographic considerations, the thermodynamic information of the adsorption process, indicative of cooperative adsorption. Notably, the behavior of the system at the molecular level obtained by diffraction experiments is in a very good agreement with the adsorption properties of the bulk material. To the best of our knowledge, this is the first time that such a detailed powder X-ray diffraction analysis is performed for porous materials, showing that it is possible to extract also thermodynamic considerations of the adsorption process. Noteworthy, this work shows a very good and encouraging agreement between the results obtained from conventional volumetric experiments and the "HR-PXRD adsorption isotherms," opening the way to an increasing level of comprehension of adsorption processes through diffraction experiments. Finally, the detailed information retrieved, at the molecular level, on this case of study might help the design of next-generation cutting-edge porous materials.

4. Experimental Section

Materials and Methods: All the solvents were dried and distilled under nitrogen by standard procedures prior to use. Unless otherwise specified, the reagents were obtained from commercial suppliers and used as received. Differential scanning calorimetry and thermogravimetric analysis were carried out simultaneously on a NETZSCH STA 409 PC Luxx instrument. About 10 mg of sample, weighed exactly to the fifth decimal digit, were placed in an alumina pan and heated under a nitrogen flow (40 mL min^{-1}). The heating ramp used was 10 K min^{-1}, from 303 to 1173 K; plots are included in Figure S1 in the Supporting Information. Elemental analyses were performed on a Perkin-Elmer 2400 instrument. The IR spectrum (Figure S4, Supporting Information) was acquired over the range of 4000–500 cm^{-1} in attenuated total reflectance (ATR) on a diamond crystal by means of a Perkin–Elmer Paragon 1000 spectrometer. Gas sorption studies were performed on a Micromeritics 3Flex instrument. N_2 sorption measurements were carried out at 77, 273, and 298 K and up to 1 bar, while CO_2 sorption measurements were carried out at 195, 273, 283, and 298 K and up to 1 bar. Sample activation was achieved through thermal activation at 393 K for 12 h under high vacuum (10^{-6} Torr). The nature and purity of all the batches of $Fe_2(BDP)_3$ isolated for the present work were assessed by combining elemental analysis, IR spectroscopy, PXRD, and N_2 adsorption at 77 K. PXRD data for qualitative analysis were acquired in the 2θ range 3°–35°, with a step of 0.02° and a time per step of 1 s, with the following procedure: gently ground powders of $Fe_2(BDP)_3$ were deposited in the 1 mm deep hollow of a quartz zero-background plate. Diffraction experiments were performed using Cu-Kα radiation (λ = 1.5418 Å) on a vertical-scan Bruker AXS D8 Advance diffractometer in θ:θ mode, equipped with a Goebel Mirror and a Bruker Lynxeye linear Position Sensitive Detector, and with the following optics: primary and secondary beam Soller slits, 2.3° and 2.5°, respectively; divergence slit, 0.1°; receiving slit, 2.82°. Generator setting: 40 kV, 40 mA. The nominal resolution for the present set-up is 0.08° 2θ (FWHM of the α_1 component) for the LaB_6 peak at about 21.3° (2θ). Whole powder pattern refinements were carried out adopting the Le Bail method,[42] as implemented in TOPAS-Academic V6,[47,48] using, as the starting point, the unit cell parameters already reported in the literature.[33] Figure S3 (Supporting Information) collects the final graphical output of a whole powder pattern refinement, as a representative example.

Synthesis of $Fe_2(BDP)_3$: $Fe_2(BDP)_3$ was synthetized according to a synthetic procedure previously reported in the literature by Herm et al. in 2013.[33] The samples were washed and thermally activated following the same procedure. Anal. calc. for $Fe_2(C_{12}N_4H_8)_3$ [$Fe_2(BDP)_3$, FW = 736.36 g mol^{-1}]: C, 58.72; H, 3.29; N, 22.83%. Found: C, 57.06; H, 3.37; N, 21.13%. FT-IR (solid, ATR, cm^{-1}, Figure S4, Supporting Information): $\nu_{C=C}$ 1578, $\nu_{C=N}$ 1386, 1343.

Variable-Temperature Powder X-ray Diffraction (VT-PXRD) Measurements and Data Treatment: The thermal behaviour of $Fe_2(BDP)_3$ was investigated by in situ VT-PXRD using a custom-made sample heater (Officina Elettrotecnica di Tenno, Ponte Arche, Italy) plugged in a Bruker AXS D8 Advance diffractometer. ≈20 mg of the as-synthesized compound were deposited in an aluminium sample-holder and heated in air from 303 K until decomposition (T = 723 K) with steps of 20 K. A PXRD pattern was acquired at each step, covering a sensible low-to-medium-angle 2θ range (6.0°–29.5°, Cu-Kα). Whole powder pattern parametric refinements of the data acquired before the loss of crystallinity, carried out with the Le Bail method, disclosed the behaviour of the unit cell parameters as a function of temperature.

Breakthrough Curve Experiments: A gas mixture of composition N_2:CO_2 = 85:15 v/v was prepared using Bronkhorst mass flow controllers and flowed at different temperatures (T = 273, 303, 323, 353 K, total gas flux 20 mL min^{-1}) into a stainless-steel column of 152 mm length and 4 mm diameter packed with 0.476 g of microcrystalline $Fe_2(BDP)_3$ using glass wool on the edges to avoid the leakage of the material. The chromatographic column was placed inside the oven of a Varian GC instrument which allows temperature control above 298 K. Lower temperatures were controlled using a Dewar bath. The relative gas mixture composition exiting the column was monitored using an OmniStar PFEIFFER VACOON residual gas mass spectrometer to detect the corresponding ion peaks at 4 (He), 28 (N_2), and 44 (CO_2) m/z value. Prior to the first measurement, the material was activated at 353 K under He flow (20 mL min^{-1}) overnight and at 423 K under He flow (20 mL min^{-1}) for 4 h; successive activation procedures between measurements at different temperatures were performed at 393 K under He flow (20 mL min^{-1}) for 20 min. The complete reactivation was monitored through the mass spectrometer.

High-Resolution Powder X-ray Diffraction (HR-PXRD) Adsorption Isotherms and Data Treatment: In situ HR-PXRD measurements were performed at the European Synchrotron Radiation Facility (ESRF, Grenoble, France; Proposals CH-5337 and CH-6073,[49] ID22 High-Resolution Powder-Diffraction Beamline) by using the gas handling system described by Brunelli et al.[20] Pre-activated $Fe_2(BDP)_3$ was gently ground and introduced into a 0.5 mm diameter borosilicate glass capillary. The capillary was first aligned, then connected to the gas handling system (PACE CM0 Standard Precision: 0.02% Rdg + 0.02% FS). The MOF was then further activated at 453 K (cryostream

precision: ±0.1 K) under high vacuum (7×10^{-6} bar) by means of a turbo vacuum pump for ≈2 h in order to remove any residual trapped solvent in its 1D channels. To minimize preferred-orientation effects and obtain very accurate diffracted intensities, the capillary-containing cell was screwed onto a motorized goniometric head that allowed ±120° rocking of the capillary with its axis colinear with that of the goniometer. All the measurements were carried out on the same capillary. The sample radiation damage was monitored and prevented by translating the capillary a total of three times during the whole experiment; an equilibration time of 15 min was adopted at each pressure point. Two different temperatures were investigated, namely T = 273 and 298 K, while varying the CO_2 loading in the pressure range of 0–8 bar, working at 35 keV (λ = 0.355 Å, calibrated with the Si NIST standard SRM 640c at room temperature) with a beam size of 1 mm (horizontal) by 0.9 mm (vertical) defined by water-cooled slits and monochromated with a cryogenically cooled Si 111 channel-cut crystal. A bank of nine detectors, each preceded by a Si 111 analyser crystal, was scanned vertically to measure the diffracted intensity. First, the space group and unit cell parameters were checked and refined through a whole powder pattern refinement carried out with the Le Bail method, starting from the reported information.[33] The Rietveld refinements on the data collected at 0 bar and T = 273 and 298 K allowed us to confirm the complete activation of the sample and were used as starting point for locating the adsorbed CO_2 molecules at higher pressures. The simulated annealing approach[50] provided the location of the primary CO_2 adsorption sites. Both crystallographically independent portions of the ligand (disordered ½ ligand and ¼ ligand) and the three crystallographically independent CO_2 molecules were modelled as rigid bodies in *z-matrix* formalism as implemented in Topas-Academic V6.[47] Fixed bond lengths and angles were used at this stage.[51,52] The position of the centre of mass, the orientation and the site occupation factors of the CO_2 molecules, together with the occupancy and the torsion angle of the disordered phenyl rings of both independent ligands, were let to vary. The instrumental contribution to the peak shape was described with the fundamental parameters approach.[53] The anisotropic peak broadening was successfully modelled by using the Stephen's description for orthorhombic space groups, taking into account both the Lorentzian and Gaussian contributions.[54] The background was modelled by a polynomial function of the Chebyshev type. Two independent refined isotropic thermal parameters (B and B_{solv}) were assigned to the metal atom and CO_2 molecules, respectively, while to the ligand atoms a higher isotropic thermal parameter, $B + 2Å^2$, was given. During the final Rietveld refinement stages, ligand bond lengths (except for the C–H distance) were let free to refine in a restrained range of values.[55] Figure S8 in the Supporting Information of the Supporting Information collects the final graphical output of a whole powder pattern and a Rietveld refinement carried out on the HR-PXRD data, as representative examples. The R_{wp} and R_p figures of merit for all the whole powder pattern and Rietveld refinements carried out on the HR-PXRD data are reported in Tables S5–S8 in the Supporting Information. Tables S9 and S10 in the Supporting Information collect the main host–guest interactions of the three independent CO_2 molecules [CO_2-1, CO_2-2, and CO_2-3 in the text] in $Fe_2(BDP)_3$ at 273 and 298 K and different CO_2 loadings, as retrieved from the Rietveld refinements carried out on the HR-PXRD data. Tables S11 and S12 (Supporting Information) collect details on the orientational disorder of the phenyl ring of the ligands in response to CO_2 loading. Finally, Tables S13 and S14 (Supporting Information) contain the occupancy values and quantity of gas adsorbed at 273 and 298 K, respectively, and at increasing CO_2 loadings.

The CO_2 molecules site occupation factors obtained by Rietveld refinement were then used to build two adsorption isotherms at 273 and 298 K in the range of the studied pressures (0–8 bar). The adsorption isotherms were then modelled using the Freundlich–Langmuir equation [Equation (1)][43]

$$n = \frac{a \cdot b \cdot p^c}{1 + b \cdot p^c} \tag{1}$$

where n is the amount adsorbed (the loading) in mmol g^{-1}, p is the pressure in kPa, a is the maximal loading in mmol g^{-1}, b is the affinity constant in 1 kPa^{-c}, and c is the heterogeneity exponent. Finally, the isosteric heats of adsorption (Q_{st}) for $Fe_2(BDP)_3$ as a function of the CO_2 uptake were calculated from the adsorption isotherms retrieved from the HR-PXRD experiment at 273 and 298 K. The calculation was performed based on the Clausius–Clapeyron equation [Equation (2)][43]

$$Q_{st} = -R\left[\Delta(\ln P) / \Delta(1/T)\right]_N \tag{2}$$

where R = ideal gas constant and N = amount of gas adsorbed in mmol g^{-1}.

Metropolis Monte Carlo Simulations: A theoretical study on the interactions of the CO_2 molecules with the framework of $Fe_2(BDP)_3$ was performed using the Materials Studio 6.0 (MS6.0) software from Accelrys, Inc.[46] Two different $Fe_2(BDP)_3$ structural configurations were considered, namely: (i) the structural model of the activated material obtained from the Rietveld refinement at 273 K and 0 bar of CO_2, and (ii) the structural model obtained from the Rietveld refinement at 273 K and 1 bar of CO_2. A double cell along the *a*-axis was used during the simulations. After the crystallographic symmetry reduction to *P*1, the primitive structures were optimized by using the "Forcite Geometry Optimization" module; more details on these calculations can be found in Table S15 in the Supporting Information. Adsorption simulations were carried out using the "Adsorption Locator" module of MS6.0. Adsorption Locator simulates a substrate loaded with an adsorbate of a fixed composition, allowing to find low energy adsorption sites. The identification of the possible adsorption configurations in $Fe_2(BDP)_3$ was carried out by Monte Carlo searches of the configurational space of the substrate-adsorbate system, slowly decreasing the temperature according to a simulated annealing schedule. The Metropolis Monte Carlo (MMC) method was used for the adsorption configurations search. The adsorbate molecules were treated as rigid bodies by allowing changes in their positions and orientations during the simulated annealing task. The simulations were carried out by inserting an increasing number of CO_2 molecules, until reaching the structure saturation (Figures S15 and S16, Supporting Information). The Monte Carlo simulation yielded several conformations of CO_2 molecules in $Fe_2(BDP)_3$. The results of the most stable conformations were presented in this work. More details on these calculations can be found in Table S16 in the Supporting Information. The two CO_2 adsorption isotherm simulations at 273 and 298 K were carried out using the "Sorption" module of MS6.0, enabling a direct comparison with the experimental observations. The Sorption module calculated the loading of the CO_2 molecules in the host framework over a range of total fugacities (see Table S17 in the Supporting Information), at the two fixed temperatures of 273 and 298 K. During the simulation, on the one hand the CO_2 molecules were randomly rotated and translated within the host framework, on the other hand they were randomly introduced and deleted from the host framework. The resulting configuration was accepted or rejected according to the selection rules of the Metropolis Monte Carlo method. The first fugacity simulation started with the same optimized empty frameworks (in *P*1 symmetry) quoted above; this result was used as starting point for the subsequent one. More details on these calculations can be found in Table S17 in the Supporting Information.

CCDC 2209131–2209150 contains the supplementary crystallographic data for this paper. These data can be obtained free of charge from The Cambridge Crystallographic Data Centre via www.ccdc.cam.ac.uk/data_request/cif.

Supporting Information

Supporting Information is available from the Wiley Online Library or from the author.

Acknowledgements

R.V. and S.T. contributed equally to this work. All authors have given approval to the final version of the manuscript. This research is part of the project "One Health Action Hub: University Task Force for the resilience of territorial ecosystems" by *Università degli Studi di Milano – PSR 2021 – GSA – Linea 6*. V.C. thanks the Italian MIUR for funding through the PRIN2017 program (project "Moscato" n° 2017KKP5ZR_004) and Università degli Studi di Milano for the Transition Grant (PSR2015-1721VCOLO_01). R.V. and S.G. acknowledge Università dell'Insubria for partial funding. R.V. acknowledges Fondazione CRUI for a one-year post-doctoral grant (Go4IT, 2020) and programa Juan de la Cierva Formación (FJC2020-045043-I). J.A.R.N. and R.V. thank MCIN/AEI/10.13039/501100011033 and European Union NextGenerationEU/PRTR (Grants PID2020-113608RB-I00; TED2021-129886B-C41); Junta de Andalucía-Conserjería de Economía y Conocimiento/EU ERDF (Project P18.RT.612). The authors are grateful to the European Synchrotron Radiation Facility for the beamtime (experiments CH-5337 and CH-6073, ID-22 High-Resolution Powder-Diffraction Beamline) and to the local contacts of ID-22 Dr. Mauro Coduri and Dr. Giorgia Confalonieri. S.G. and R.V. acknowledge the help of Miss Laura De Filippi.

Conflict of Interest

The authors declare no conflict of interest.

Data Availability Statement

The data that support the findings of this study are available from the corresponding author upon reasonable request.

Keywords

CO_2 adsorption, cooperative adsorption, metal–organic frameworks, Monte Carlo simulations, pyrazolates, stability, synchrotron radiation

Received: October 26, 2022
Revised: January 10, 2023
Published online:

[1] Z. Ji, H. Wang, S. Canossa, S. Wuttke, O. M. Yaghi, *Adv. Funct. Mater.* **2020**, *30*, 2000238.
[2] C. Gropp, S. Canossa, S. Wuttke, F. Gándara, Q. Li, L. Gagliardi, O. M. Yaghi, *ACS Cent. Sci.* **2020**, *6*, 1255.
[3] J. Marreiros, R. de Oliveira-Silva, P. Iacomi, P. L. Llewellyn, R. Ameloot, D. Sakellariou, *J. Am. Chem. Soc.* **2021**, *143*, 8249.
[4] M. Thommes, K. Kaneko, A. V Neimark, J. P. Olivier, F. Rodriguez-Reinoso, J. Rouquerol, K. S. W. Sing, *Pure Appl. Chem.* **2015**, *87*, 1051.
[5] J. W. M. Osterrieth, J. Rampersad, D. Madden, N. Rampal, L. Skoric, B. Connolly, M. D. Allendorf, V. Stavila, J. L. Snider, R. Ameloot, J. Marreiros, C. Ania, D. Azevedo, E. Vilarrasa-Garcia, B. F. Santos, X. Bu, Z. Chang, H. Bunzen, N. R. Champness, S. L. Griffin, B. Chen, R. Lin, B. Coasne, S. Cohen, J. C. Moreton, Y. J. Colón, L. Chen, R. Clowes, F. Coudert, Y. Cui, et al, *Adv. Mater.* **2022**, *34*, 2201502.
[6] H. Pfeifer, *Phys. Rep.* **1976**, *26*, 293.
[7] H. Pfeifer, in *NMR Basic Principles and Progress/NMR Grundlagen Und Fortschritte* (Eds: P. Diehl, E. Fluck, R. Kosfeld), Springer, Berlin/Heidelberg, Germany **1972**, pp. 53–153.
[8] M. Watanabe, T. Itō, *Jpn. J. Appl. Phys.* **1980**, *19*, 1863.
[9] A. Kondor, A. Dallos, *J. Chromatogr. A* **2014**, *1362*, 250.
[10] C. Tisserand, R. Calvet, S. Patry, L. Galet, J. A. Dodds, *Powder Technol.* **2009**, *190*, 53.
[11] S. O. Slavova, A. A. Sizova, V. V Sizov, *Phys. Chem. Chem. Phys.* **2020**, *22*, 22529.
[12] W. Jeong, J. Kim, *J. Phys. Chem. C* **2016**, *120*, 23500.
[13] M. Polisi, J. Grand, R. Arletti, N. Barrier, S. Komaty, M. Zaarour, S. Mintova, G. Vezzalini, *J. Phys. Chem. C* **2019**, *123*, 2361.
[14] L. Ohlin, P. Bazin, F. Thibault-Starzyk, J. Hedlund, M. Grahn, *J. Phys. Chem. C* **2013**, *117*, 16972.
[15] N. Mosca, R. Vismara, J. A. Fernandes, G. Tuci, C. Di Nicola, K. V. Domasevitch, C. Giacobbe, G. Giambastiani, C. Pettinari, M. Aragones-Anglada, P. Z. Moghadam, D. Fairen-Jimenez, A. Rossin, S. Galli, *Chem. – Eur. J.* **2018**, *24*, 13170.
[16] C. Giacobbe, E. Lavigna, A. Maspero, S. Galli, *J. Mater. Chem. A* **2017**, *5*, 16964.
[17] J. Lill, C. Dejoie, C. Giacobbe, A. N. Fitch, *J. Phys. Chem. C* **2022**, *126*, 2214.
[18] N. Hanikel, X. Pei, S. Chheda, H. Lyu, W. Jeong, J. Sauer, L. Gagliardi, O. M. Yaghi, *Science* **2021**, *374*, 454.
[19] H. S. Cho, J. Yang, X. Gong, Y. B. Zhang, K. Momma, B. M. Weckhuysen, H. Deng, J. K. Kang, O. M. Yaghi, O. Terasaki, *Nat. Chem.* **2019**, *11*, 562.
[20] M. Brunelli, A. N. Fitch, *J. Synchrotron Radiat.* **2003**, *10*, 337.
[21] L. Braglia, F. Tavani, S. Mauri, R. Edla, D. Krizmancic, A. Tofoni, V. Colombo, P. D'Angelo, P. Torelli, *J. Phys. Chem. Lett.* **2021**, *12*, 9182.
[22] D. E. Jaramillo, D. A. Reed, H. Z. H. Jiang, J. Oktawiec, M. W. Mara, A. C. Forse, D. J. Lussier, R. A. Murphy, M. Cunningham, V. Colombo, *Nat. Mater.* **2020**, *19*, 517.
[23] P. Mishra, H. P. Uppara, B. Mandal, S. Gumma, *J. Chem. Eng. Data* **2012**, *57*, 2610.
[24] N. Muroyama, A. Yoshimura, Y. Kubota, K. Miyasaka, T. Ohsuna, R. Ryoo, P. I. Ravikovitch, A. V Neimark, M. Takata, O. Terasaki, *J. Phys. Chem. C* **2008**, *112*, 10803.
[25] S. Bin Baek, D. Moon, R. Graf, W. J. Cho, S. W. Park, T.-U. Yoon, S. J. Cho, I.-C. Hwang, Y.-S. Bae, H. W. Spiess, *Proc. Natl. Acad. Sci. USA* **2015**, *112*, 14156.
[26] Y. Chen, Z.-L. Shi, L. Wei, B. Zhou, J. Tan, H.-L. Zhou, Y.-B. Zhang, *J. Am. Chem. Soc.* **2019**, *141*, 3298.
[27] J. Oktawiec, H. Z. H. Jiang, J. G. Vitillo, D. A. Reed, L. E. Darago, B. A. Trump, V. Bernales, H. Li, K. A. Colwell, H. Furukawa, *Nat. Commun.* **2020**, *11*, 3087.
[28] B. Felsner, V. Bon, J. D. Evans, F. Schwotzer, R. Grünker, I. Senkovska, S. Kaskel, *Chem. - Eur. J.* **2021**, *27*, 9708.
[29] D. Lenzen, J. G. Eggebrecht, P. G. M. Mileo, D. Fröhlich, S. Henninger, C. Atzori, F. Bonino, A. Lieb, G. Maurin, N. Stock, *Chem. Commun.* **2020**, *56*, 9628.
[30] H. Sung Cho, H. Deng, K. Miyasaka, Z. Dong, M. Cho, A. V Neimark, J. Ku Kang, O. M. Yaghi, O. Terasaki, *Nature* **2015**, *527*, 503.
[31] S. Lee, H. B. Bürgi, S. A. Alshmimri, O. M. Yaghi, *J. Am. Chem. Soc.* **2018**, *140*, 8958.
[32] M. I. Gonzalez, J. A. Mason, E. D. Bloch, S. J. Teat, K. J. Gagnon, G. Y. Morrison, W. L. Queen, J. R. Long, *Chem. Sci.* **2017**, *8*, 4387.
[33] Z. R. Herm, B. M. Wiers, J. A. Mason, J. M. van Baten, M. R. Hudson, P. Zajdel, C. M. Brown, N. Masciocchi, R. Krishna, J. R. Long, *Science* **2013**, *340*, 960.
[34] Z. Wang, A. Bilegsaikhan, R. T. Jerozal, T. A. Pitt, P. J. Milner, *ACS Appl. Mater. Interfaces* **2021**, *13*, 17517.
[35] S. Yuan, L. Feng, K. Wang, J. Pang, M. Bosch, C. Lollar, Y. Sun, J. Qin, X. Yang, P. Zhang, *Adv. Mater.* **2018**, *30*, 1704303.
[36] J. Perego, C. X. Bezuidenhout, A. Pedrini, S. Bracco, M. Negroni, A. Comotti, P. Sozzani, *J. Mater. Chem. A* **2020**, *8*, 11406.

[37] V. Colombo, S. Galli, H. J. Choi, G. D. Han, A. Maspero, G. Palmisano, N. Masciocchi, J. R. Long, *Chem. Sci.* **2011**, *2*, 1311.
[38] N. Biggins, M. E. Ziebel, M. I. Gonzalez, J. R. Long, *Chem. Sci.* **2020**, *11*, 9173.
[39] M. L. Aubrey, B. M. Wiers, S. C. Andrews, T. Sakurai, S. E. Reyes-Lillo, S. M. Hamed, C.-J. Yu, L. E. Darago, J. A. Mason, J.-O. Baeg, *Nat. Mater.* **2018**, *17*, 625.
[40] A. J. Howarth, Y. Liu, P. Li, Z. Li, T. C. Wang, J. T. Hupp, O. K. Farha, *Nat. Rev. Mater.* **2016**, *1*, 15018.
[41] The decomposition temperature obtained from STA should be considered more reliable than the one obtained from VT-PXRD studies.
[42] A. Le Bail, H. Duroy, J. L. Fourquet, *Mater. Res. Bull.* **1988**, *23*, 447.
[43] A. Nuhnen, C. Janiak, *Dalt. Trans.* **2020**, *49*, 10295.
[44] A. L. Myers, J. M. Prausnitz, *AIChE J.* **1965**, *11*, 121.
[45] Q. Yang, C. Zhong, *J. Phys. Chem. B* **2005**, *109*, 11862.
[46] BIOVIA, Dassault Systèmes,Biovia Materials Studio 6.0, San Diego: Dassault Systèmes, **2018**.
[47] A. A. Coelho, *TOPAS-Academic V6* **2016**, http://www.topas-academic.net.
[48] A. A. Coelho, *J. Appl. Crystallogr.* **2018**, *51*, 210.
[49] R. Vismara, S. Galli, S. Terruzzi, V. Colombo, "Unveiling the CO_2 adsorption sites in the triangular channels of $Fe_2(BDPNH_2)$ metal-organic framework by in situ HR-PXRD [Data set].," https://doi.org/10.15151/ESRF-ES-517791935, **2021**.
[50] A. A. Coelho, *J. Appl. Crystallogr.* **2000**, *33*, 899.
[51] Bond lengths and angles for the rigid body describing the ligand: C-C and C-N of the pyrazolate ring 1.38 Å; C-H of the pyrazolate ring 0.95 Å; pyrazolate ring internal and exter-nal bond angles 108° and 126°, respectively; C-C and C-H of the phenyl ring.
[52] Rigid body modelling for CO_2: C=O 1.21 Å; O=C=O 180°.
[53] R. W. Cheary, A. A. Coelho, *J. Appl. Crystallogr.* **1998**, *31*, 851.
[54] J.-H. Her, P. W. Stephens, Y. Gao, G. L. Soloveichik, J. Rijssenbeek, M. Andrus, J.-C. Zhao, *Acta Crystallogr* **2007**, *63*, 561.
[55] Refined bond lengths in the final stages of the Rietveld refinements: exocyclic C–C 1.44–1.50 Å; C–C and C–N of the pyrazolate ring 1.32–1.42 Å; C–C of the benzene ring 1.34–1.43 Å.